Structural, magnetic, and magnetotransport properties of Mn-Si films synthesized on a 4*H*-SiC(0001) wafer

Wenhong Wang,* Fumiyoshi Takano, and Hiro Akinaga
Nanotechnology Research Institute (NRI), National Institute of Advanced Industrial Science and Technology (AIST), 1-1-1 Umezono, Tsukuba, Ibaraki 305-8568, Japan

Hironori Ofuchi
Japan Synchrotron Radiation Research Institute (JASRI), 1-1-1 Kouto, Sayo-cho, Sayo-gun, Hyogo 679-5198, Japan
(Received 7 November 2006; revised manuscript received 26 December 2006; published 25 April 2007)

We present a comprehensive study of the structural, magnetic, and magnetotransport properties of Mn-Si films synthesized on a 4*H*-SiC(0001) wafer by an annealing method. Magnetic- and fluorescence-extended x-ray-absorption fine-structure measurements reveal that the sample comprises two uncoupled magnetic phases: one is the top synthesized Mn-Si layer, which displays a Curie temperature around 300 K and magnetic anisotropy; the other one is Mn atoms, which solely incorporate on the interstitial site in the 4*H*-SiC lattice in the interface and show superparamagnetismlike behavior with a blocking temperature below 2 K. The magnetoresistance (MR) exhibits an interesting temperature- and field-dependent behavior. At temperatures above 100 K, the sample only exhibits a positive MR. At temperatures below 100 K, a negative MR prevails. Interestingly, at intermediate temperature of 100 K, with increasing magnetic field, a sign inversion of the MR from negative to positive is observed. The possible origin of the positive and negative MR is discussed. Furthermore, we found that the Hall effect is dominated by an anomalous Hall effect (AHE) due to side jumps at temperatures between 2 K and 100 K. However, at temperatures higher than 100 K, the AHE cannot be described with either a skew scattering or side jumps mechanism.

DOI: 10.1103/PhysRevB.75.165323 PACS number(s): 75.50.Pp, 75.70.−i, 75.47.−m, 61.10.Ht

I. INTRODUCTION

New materials that exhibit both room-temperature ferromagnetism and semiconducting properties are necessary for spintronic devices. Diluted magnetic semiconductors (DMSs), in which magnetic atoms are randomly substituted for the semiconductor atoms, are expected to be the most promising candidates to meet this requirement.[1,2] Since the discovery of a ferromagnetic order in Mn-doped InAs in 1992 by Ohno *et al.*,[3] many other ferromagnetic DMSs have been discovered, mostly III-V and II-V types.[1,4] Recently, a Curie temperature (T_c) up to 173 K has been achieved in Mn-doped GaAs and intense efforts have been made to reach a T_c higher than room temperature.[5–8] On the other hand, it is highly desired that ferromagnetic DMSs be fabricated with the most widely used conventional elemental semiconductors (i.e., Si and Ge) by appropriate doping with transition metal ions such as Mn. Spintronic devices based on conventional elemental semiconductors are believed to be significant due to the mature processing technology in modern electronics. Therefore, there have been many attempts to fabricate new materials such as Mn-doped Si and Ge as ferromagnetic DMSs[9,10] and, mostly in recent years, to try different ways to grow ferromagnetic Mn_xSi_{1-x} or Mn_xGe_{1-x} thin films on Si or Ge semiconductors by molecular beam epitaxy with a potential use in spintronics.[11–15]

Silicon carbide (SiC) is known to be one of the most useful semiconductors for electronic device applications, because it has a higher electric breakdown field and larger band gap than Si. Surprisingly, compared with the large amount of attempts to grow crystalline ferromagnetic Mn_xSi_{1-x} thin films on Si substrates, there have been very few attempts to grow ferromagnetic layers on SiC substrates, although such ferromagnetic/semiconductor structures have great potential for future electronic and optoelectronic devices.[16,17] Fortunately, interest in exploring SiC-based ferromagnetic DMSs has been reinforced and some prior works have been carried out both experimentally and theoretically.[18,19] The initial aim of our work is to synthesize and investigate SiC:Mn films as other candidates for SiC-based DMSs. In our preliminary studies,[20] we have synthesized Mn-Si-related compounds on a 4*H*-SiC homoepitaxial wafer by using an annealing method. It has been found that synthesized Mn-Si films showed a T_c of 300 K, although x-ray diffraction (XRD) and selected-area diffraction (SAD) measurements suggested that paramagnetic tetragonal Mn_5Si_2 was dominant.[21] As the origin of room-temperature ferromagnetism, it is suggested that a small amount of carbon atoms incorporated into the paramagnetic Mn_5Si_2 host and induced the ferromagnetic order in Mn_5Si_2.[20]

Carbon-induced room-temperature ferromagnetic order in paramagnetic Mn_5Si_2 is reminiscent of the ferromagnetic order reported by Takeuchi *et al.*[22] in annealed Mn/C/Si triple layers and by Nakatani *et al.*[23] in annealed C/Mn/C/Si multilayers prepared by sequential deposition on Si. In these triple layers or multilayers, some unknown intermediate complex phases were considered to be formed at the interfaces since neither the Mn/Si nor Mn/C bilayers support ferromagnetism above room temperature. More recently, Sügers *et al.*[24,25] reported that $Mn_5Si_3C_x$ films prepared by magnetron sputtering at Si(001) substrates have a T_c of 325 K in contrast to antiferromagnetic Mn_5Si_3. The origin of the ferromagnetism was explained as the effect of the anisotropic modification of the local structure around the manga-

 ©2007 The American Physical Society

nese (Mn) sites by carbon (C) atoms. These results strongly suggest that carbon-incorporated Mn-Si might be one of the most promising candidates for novel spintronic materials due to its full compatibility with the mainstream of Si technology.

However, to realize the potential of these carbon-incorporated Mn-Si films for spintronic devices, it is essential to explore their magnetic and transport properties and their interface structure between ferromagnetic layers and semiconductor surfaces. In this paper we present a comprehensive study of ferromagnetism and electrical transport in carbon-incorporated Mn_5Si_2 films synthesized on wurtzite 4*H*-SiC(0001) substrates by an annealing method. In addition, fluorescence-extended x-ray absorption fine-structure (EXAFS) measurements were performed to elucidate the relationship between the local structures around Mn atoms and the magnetic and transport properties.

II. EXPERIMENTAL ASPECTS

The 4*H*-SiC homoepitaxial wafer used as a substrate has a 5-μm SiC epitaxial layer on a 4*H*-SiC(0001) substrate off-oriented 8° towards $\langle 11\bar{2}0\rangle$.[26] The SiC epitaxial layer shows *n*-type conduction, and the carrier density was evaluated to be $\sim 1\times 10^{15}$ cm^{-3}. The typical size of the substrates is 10 mm × 10 mm. Growth of Mn was carried out in an ultrahigh-vacuum (UHV) multichamber molecular-beam epitaxy system (Eiko Engineering Ltd.). Before Mn growth, the SiC substrate was thermally cleaned at 1000 °C for 10 min to remove the thin oxide layer on the surface. Then Mn with a thickness of 50 nm was deposited on the clean 4*H*-SiC substrates using a Knudsen cell in the growth chamber. We have investigated the growth of full epitaxial Mn films on the 4*H*-SiC(0001), using substrate temperatures as low as 300 °C. In the growth of Mn films, we found that the best crystalline quality was achieved at a substrate temperature of 300 °C.[27] Then the substrate temperature was kept at 300 °C during Mn deposition. The growth rate was set to 20 nm/h. The Mn cell temperature was kept at 800 °C during growth. After Mn deposition, *in situ* annealing was performed at 1000 °C for 3 min to diffuse the Mn atoms into the SiC homoepitaxial layer.

The structural properties of the sample were investigated by *ex situ* XRD with Cu $K\alpha$ radiation. The cross-sectional transmission electron microscope (TEM) images indicated that a synthesized layer about 100 nm thick is found to have been obtained for the sample.[20] Also the TEM SAD results suggested that Mn_5Si_2 is dominant in all samples.[20] Note that from our TEM and XRD data, we could not identify additional Mn-Si cluster phases, which possibly formed in our structures. The EXAFS measurements were performed at beamline BL12C at the Photon Factory in Tsukuba with a Si(111) double-crystal monochromator and a bent cylindrical mirror using synchrotron radiation from the 2.5-GeV storage ring. The EXAFS spectra were measured in the fluorescence-detection mode. The intensity of incident x-ray beam was monitored by a nitrogen-filled ionization chamber, while the x-ray fluorescence signal was detected by an array of 19 elements of Ge solid-state detectors. All EXAFS measurements were performed at 70 K in order to reduce thermal vibration.

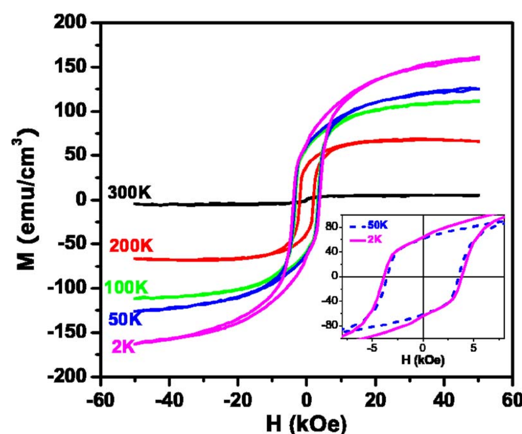

FIG. 1. (Color online) Magnetization hysteresis loops of synthesized film measured at various temperatures. The inset shows an expanded region of the loop obtained at 2 and 50 K, respectively.

The magnetization measurements up to 380 K were done in a Quantum Design superconducting quantum interference device (SQUID) magnetometer. All data presented here were collected for the diamagnetic background of the substrate according to the following procedure: We measured the magnetization of the respective sample up to the highest magnetic field available (5 T). At this high field, the diamagnetic contribution from SiC dominates the signal. A linear fit yields the slope of the signal at high fields, which in all cases was virtually identical to that of bare SiC substrates. A straight line with the slope determined from the fit was then subtracted from the raw data. Prior to measuring the temperature dependence of the magnetization, the sample was first cooled from room temperature to 2 K either under a saturation field of 20 kOe [field cooled (FC)] or at zero field [zero-field cooled (ZFC)]. In the case of ZFC measurements the sample is demagnetized under an oscillatory magnetic field at room temperature before cooling it down to 2 K. The magnetotransport measurements were performed at various temperatures between 2 and 300 K using a physical property measurement system (PPMS).

III. RESULTS AND DISCUSSION

A. Magnetization

Figure 1 shows the magnetization loops obtained at temperatures of 2, 50, 100, 200, and 300 K, respectively. The magnetic field was applied along the film plane. At all temperatures, the magnetization saturates at high magnetic fields and exhibits a hysteresis at lower fields. These two features indicate ferromagnetic behavior. When examined closely it is clear that the shape of the hysteresis loop at 2 K is different from the rest. The lower-right inset of Fig. 1 shows an expanded region of the hysteresis loop obtained at 2 and 50 K, respectively. The loop obtained at 2 K appears to be a superposition of two loops with different coercive fields (H_c) and remanent magnetization (M_r), indicating that there might be two uncoupled magnetic phases present in the sample, one of

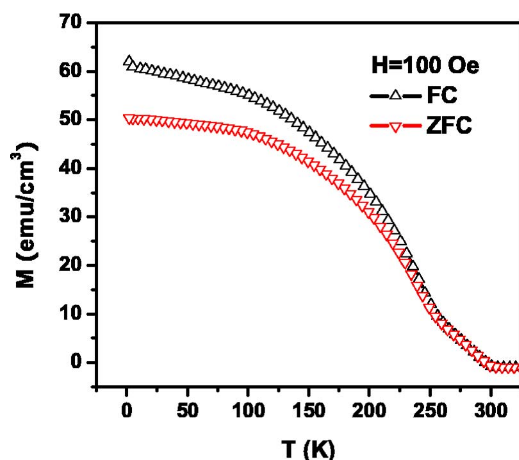

FIG. 2. (Color online) Temperature-dependent ZFC and FC magnetization under a magnetic field of 100 Oe.

which has a very low transition temperature below 2 K, while the other one exhibits ferromagnetism up to room temperature.

Figure 2 shows the temperature dependence of FC and ZFC magnetization under a magnetic field of 100 Oe. It is clear from this figure that the FC and ZFC curves are qualitatively similar. The two curves remain separated throughout the entire temperature range 2–300 K, while they coincide at around 300 K. The separation between the FC and ZFC curves indicates a hysteretic behavior, which is consistent with our observation shown in Fig. 1. The two curves coincide at the Curie temperature T_c, when the hysteresis disappears. Clearly, T_c is around 300 K for the sample. Since the applied field was only 100 Oe for the measurement of the magnetization, the FC curve is expected to qualitatively represent the temperature dependence for M_r. The second steep increase of magnetization at 2 K in the FC curve is consistent with our observation of an abnormal magnetic loop to be around that temperature, indicating that two magnetic phases may coexist in the system.

We also measured the saturation magnetization (M_s) as a function of temperature over the range 2–380 K, as shown in Fig. 3. As a result, we found that the temperature dependence of magnetization in saturation could be described, within a reasonable limit and at low temperature (2–100 K), by the Bloch formula $M_s(T)=M_s(0)(1-bT^{3/2})$, where $M_s(0)$ and the spin-wave parameter b depend on the film thickness. As is shown in the inset of Fig. 3, fitting the data to this formula yields the best fit for a b value of $1.25\pm0.31 \times 10^{-4}$ K$^{-3/2}$. The magnetization shows a $T^{3/2}$ dependence at low temperature. At temperatures above 100 K, however, we found that the M_s deviates from the $T^{3/2}$ dependence and becomes linear with T^2. That is, $M_s(T)$ can be expressed empirically as a function of temperature as $M_s(T)=M_s(0)[1-(T/T_c)^2]^{1/2}$. This fit gives a ferromagnetic transition temperature $T_c=300$ K, as shown in Fig. 3. This calculated T_c is well consistent with the experimental one obtained from the temperature-dependent magnetization curve. This kind of progressive change of the character of magnetism from localized moments (Heisenberg type) and collective spin excitations at low temperature (the magnetization varies as $T^{3/2}$)

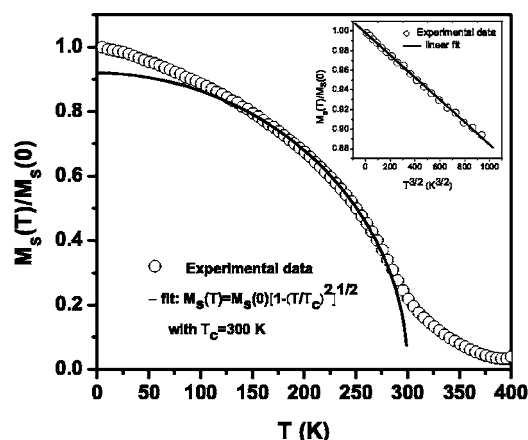

FIG. 3. Temperature-dependent saturation magnetization M_s. The inset shows the data of M as a function of $T^{3/2}$ for $T<100$ K. The solid line in the inset graph is a linear fit to the data, demonstrating the $T^{3/2}$ dependence of magnetization for this low-T range. At $T>100$ K, the data can be fitted by $M_s(T)=M_s(0)[1-(T/T_c)^2]^{1/2}$ with $T_c=300$ K.

to itinerant at high temperatures (the magnetization varies more as T^2) was previously observed for many Heusler alloys, such as NiMnSb,[28] Ni_2FeGa,[29] and Co_2MnSi.[30] The transition was interpreted as a result of individual Stoner excitations forbidden at low temperatures due to the half metal gap between the Fermi energy and the bottom of the spin-down band.

Figure 4 shows the magnetic field dependence of "in-plane" ($H_\parallel$) and "out-of-plane" ($H_\perp$) magnetization (M-H curves) measured at 2 K. The hysteresis loops clearly show magnetic anisotropy. However, in order to determine the easiest axis of our Mn-Si film, angle-dependent magnetization measurements are needed. Nevertheless, at this stage, we can claim that the in-plane magnetization is easier than the out-of-plane one. The magnetization of the film is therefore dominated by the shape anisotropy. In this case, the saturation magnetization $M_s=165$ emu/cm^3, remnant magnetization $M_r=65$ emu/cm^3, and coercivity $H_c=3.9$ kOe for

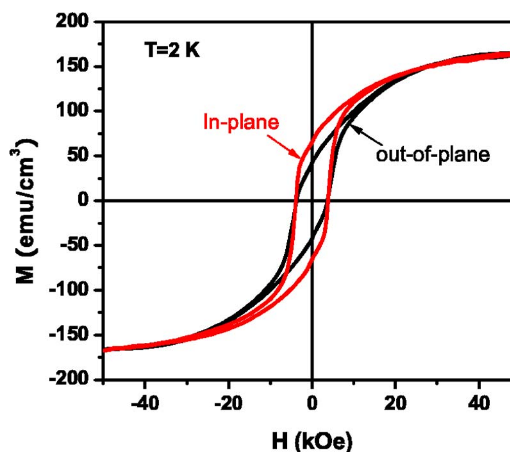

FIG. 4. (Color online) Magnetic hysteresis loops with the magnetic field applied parallel and perpendicular to the sample plane. Measurements were made at 2 K.

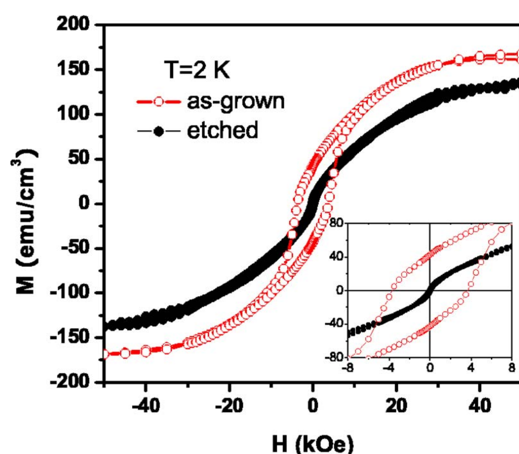

FIG. 5. (Color online) Magnetic hysteresis loops of samples before and after etching. The magnetic field was applied perpendicular to the sample plane. The inset shows the loop at small magnetic fields.

the in-plane loop, whereas M_r=43 emu/cm^3 and H_c =3.7 kOe for the out-of-plane loop. For a single-domain film, the magnetostatic energy density contains contributions from the demagnetizing field, uniaxial anisotropy, and Zeeman energy. From the in-plane saturation field (H_s) and the relation $K=m_sH_s/2V$,[31] where V is the magnetic volume of the film and m_s is its measured saturation moment, we find the uniaxial anisotropy constant $K=2.66\times10^5$ J/m^3.

In the following, we will discuss briefly the magnetism near the interface. For this study, the thickness of the top synthesized Mn_5Si_2 layer was reduced gradually by chemical etching. The etchant is dilute hydrochloric acid (~10%). In Fig. 5, we show the magnetization loops obtained at 2 K for samples before and after etching. Very interestingly, when the top synthesized Mn_5Si_2 layer was removed completely (named the etched sample hereafter), the etched sample shows a superparmagnetismlike behavior; that is, both M_r and H_c reduce to zero (see the inset of Fig. 5). It means that the blocking temperature is lower than 2 K. Based on this simple decomposition and previous magnetic measurements, we propose that there are two uncoupled magnetic phases in our sample: one is the top synthesized layer—namely, carbon-incorporated intermetallic compound Mn_5Si_2—which displays a T_c around 300 K; the other one is an unknown superparamagnetismlike phase with a blocking temperature below 2 K.

B. Extended x-ray-absorption fine-structure studies

In order to investigate the interface geometric structures, we have performed the fluorescence EXAFS measurements. Figure 6(a) shows the Mn *K*-edge $k^2(k)$ EXAFS oscillation for the as-grown and etched samples. It is found that the feature of each EXAFS oscillation is different in the range of higher wave number. In Fig. 6(b), we also show the theoretical calculated Mn *K*-edge EXAFS oscillation function $k^2\chi(k)$ spectra for Mn_5Si_2 and cubic Mn under different mixture ratios. Apart from differences in the range $k>8$ $Å^{-1}$ the experimental spectrum of the as-grown film shows a similar

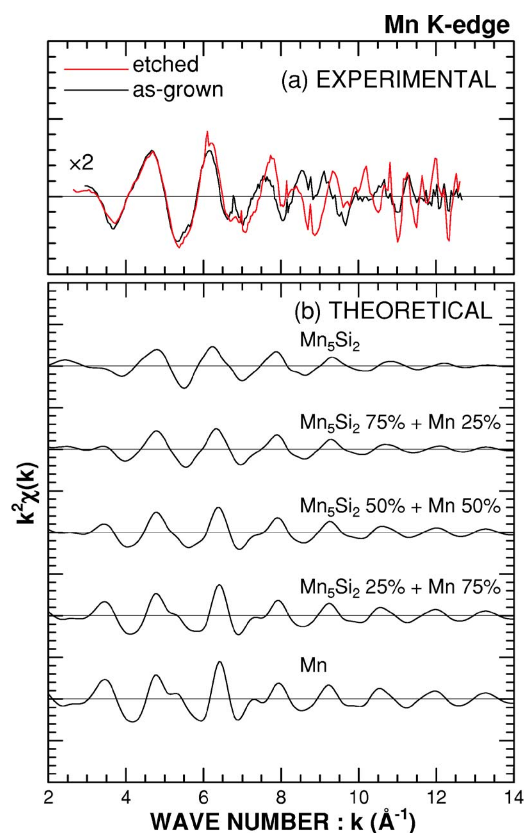

FIG. 6. (Color online) Mn *K*-edge EXAFS oscillation function $k^2\chi(k)$ spectra for (a) the as-grown and etched samples and (b) the theoretical calculated Mn *K*-edge EXAFS oscillation function $k^2\chi(k)$ spectra for Mn_5Si_2 and cubic Mn under different mixture ratio. The Debye-Waller factor was assumed to be 0.075 Å for a bond length below 4.0 Å and to be 0.100 Å for a bond length above 4.0 Å. The theoretical EXAFS data were generated by FEFF8.

behavior compared to the theoretical calculated Mn_5Si_2 spectrum, which confirms the presence of the Mn_5Si_2 phase in the film as already deduced from x-ray diffraction and selected-area diffraction measurements.[20] Moreover, for the cases of the coexistence of Mn_5Si_2 and cubic Mn, all the theoretical calculated spectra are distinctly different from the experimental one for the whole range of $k=2-12$ $Å^{-1}$.

In general, the Fourier transform allows a separation of the different configuration shells versus radial distance from the absorbing atom. In order to analyze the local atomic order in more detail, the EXAFS oscillation function $k^2\chi(k)$ spectra were Fourier transformed. Figure 7(a) shows the Fourier-transform Mn *K*-edge EXAFS spectra for the as-grown and etched samples. For the as-grown sample, double peaks were observed at R= 1.6 and 2.2 Å, and the position of the latter peak was close to that of Mn_5Si_2 in Fig. 7(b). For the etched sample, a single peak was observed at R=1.8 Å. From the curve fitting,[32] it is found that the EXAFS spectrum for the as-grown sample is fitted well by supposing the spectra of the etched sample and Mn_5Si_2. It indicates that the Mn-Si layer, which was removed by etching, forms Mn_5Si_2 mainly, and the Mn atoms incorporated in the interlayer form the other structure. Therefore, it is imperative to examine the possible position of these Mn atoms in the 4*H*-SiC lattice. In

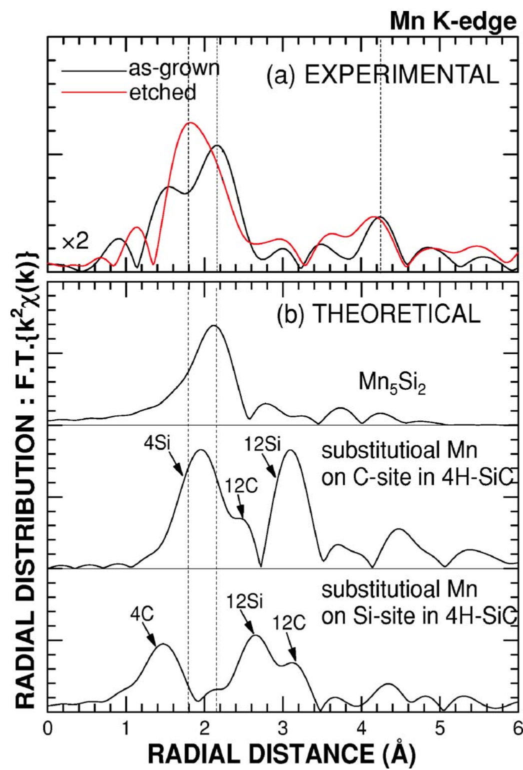

FIG. 7. (Color online) Fourier transform of Mn K-edge EXAFS oscillation function $k^2\chi(k)$ spectra for (a) the as-grown and etched samples and (b) the theoretical calculations of the Fourier transform of $k^2\chi(k)$ for Mn_5Si_2, the substitutional Mn atom on the C and Si sites in the 4H-SiC lattice. The Fourier transformation was performed in the k range of 3.0–12.0 Å^{-1}. The Debye-Waller factor was assumed to be 0.075 Å for a bond length below 4.0 Å and to be 0.100 Å for a bond length above 4.0 Å. The theoretical EXAFS data were generated by FEFF8.

Fig. 7(b) we show the theoretically calculated Fourier transform of $k^2\chi(k)$ EXAFS spectra for Mn atoms in various lattice positions including substitutionally on Si and C sites in the 4H-SiC lattice. Here we should point out that for the calculated EXAFS data, a reliable result for the second-coordination shell could not be obtained due to the large number of different atom sites and therefore scattering paths, which results in a large number of free parameters. In this case, therefore, the comparison was performed by restriction to the first-coordination-shell range R=1.0–3.2 Å. Clearly all the spectra are distinctly different from the experiment spectrum of the etched sample. Thus, it is considered that the Mn atoms in the etched sample do not substitute on Si or C sites in the 4H-SiC lattice.

We now discuss the possibility of Mn atoms incorporated into the interstitial site in the 4H-SiC lattice. In Fig. 8(a) we show a schematic illustration of the possible position of Mn atoms in an interstitial site in the Wurtzite-type crystal structure of the 4H-SiC lattice. Figure 8(b) show the Fourier transform of Mn K-edge EXAFS oscillation function $k^2\chi$(k) spectra for (i) the etched sample and (ii) theoretical calculations of the Fourier transform of $k^2\chi$(k) for the interstitial Mn atoms in various positions z (0–1.7 Å) as shown in Fig. 8(a). As a result, we found that, in the first-coordination-shell

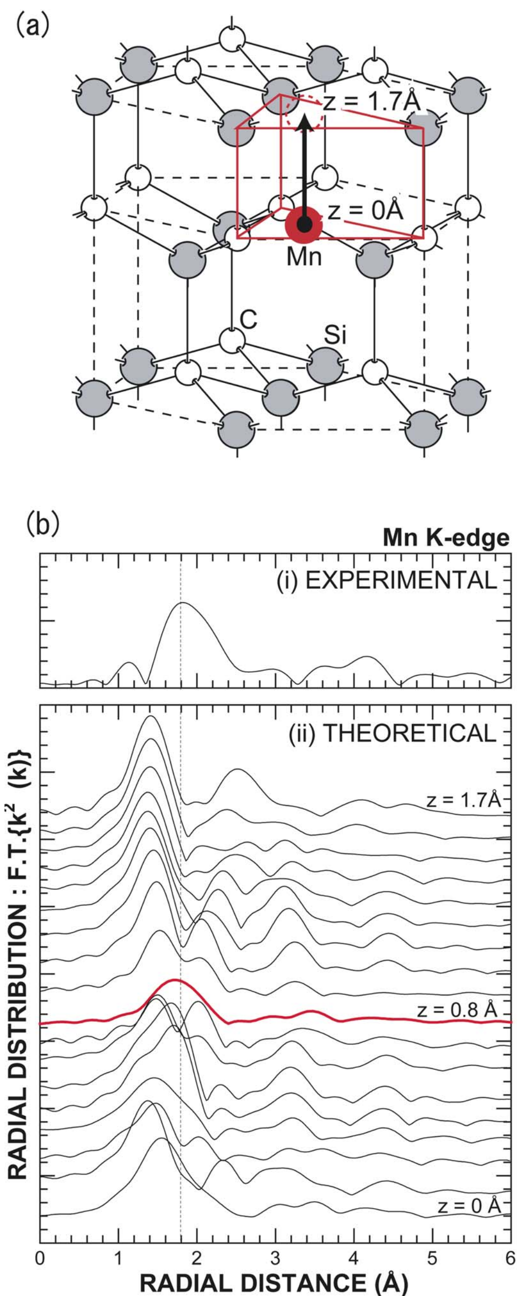

FIG. 8. (Color online) (a) Wurtzite-type crystal structure of 4H-SiC bulk. A schematic illustration of the possible position of Mn atoms in an interstitial site in the 4H-SiC lattice. (b) Fourier transform of Mn K-edge EXAFS oscillation function $k^2\chi(k)$ spectra for (i) the etched sample and (ii) the theoretical calculations of the Fourier transform of $k^2\chi(k)$ for the interstitial Mn atoms in various positions z (0–1.7 Å). The Fourier transformation was performed in the k range of 3.0–12.0 Å^{-1}. The Debye-Waller factor was assumed to be 0.075 Å for a bond length below 4.0 Å and to be 0.100 Å for a bond length above 4.0 Å. The theoretical EXAFS data were generated by FEFF8.

range R=1.0–3.2 Å, the experimental spectrum of the etched sample corresponds well to the theoretical one for z=0.8 Å. Thus, it is considered that the majority of Mn atoms in the interlayer are incorporated into the interstitial site in the 4H-SiC lattice.

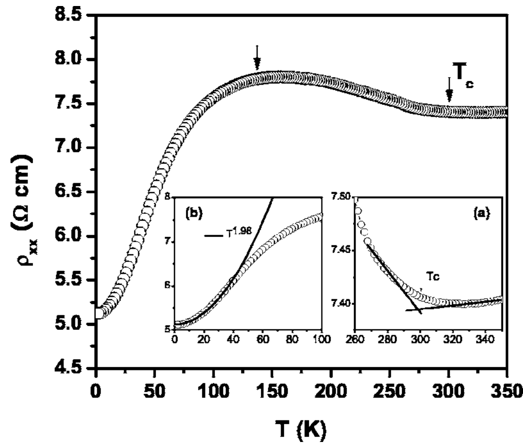

FIG. 9. Temperature-dependent zero-field longitudinal resistivity. The inset (a) shows the resistivity at temperature around T_c, and (b) shows the resistivity at the low-temperature region and the data are fitted to the $T^{1.98}$ law.

Again, the EXAFS analysis revealed that in the synthesized sample two kinds of local structures coexist. One is the top Mn_5Si_2 layer, which is also confirmed by our previous TEM and x-ray measurements.[20] The other is the isolated Mn atom in the interlayer between the Mn_5Si_2 layer and the SiC layer. Clearly, the EXAFS result is in fact consistent with our above-mentioned results of magnetic measurements. Moreover, these isolated Mn atoms are most likely responsible for the observed superparametismlike behavior in the etched sample. However, we cannot explain why these isolated Mn atoms may show the observed superparametismlike behavior, since our EXAFS data indicate that the Mn atom is an "inert" interstitial atom in the 4*H*-SiC lattice rather than participates in the chemical bonding to Si or C. Therefore, an actual understanding of the magnetic behavior observed in the present paper will require detailed *ab initio* studies, which are now in progress.

C. Magnetoresistance

Figure 9 shows the temperature dependence of the zero-field resistivity ρ_{xx}. The evolution of the resistivity is somewhat complex: the resistivity first decreases slowly with decreasing temperature, but shows a kink at $T_c \approx 300$ K, at which point the slope changes sign from positive to negative as shown inset (a) of Fig. 9; with further decreasing temperature, a broader local maximum is observed at around 120 K marked by an arrow in the temperature dependence of the resistivity. Usually, the presence of a maximum in ρ_{xx} indicates that the transport in this temperature range is strongly influenced by scattering effects, but since this broader low-temperature peak locates far below T_c, the effect of magnetic critical scattering is relatively weak. Finally, the resistivity decreases with decreasing temperature, as shown in inset (b) of Fig. 9; we found that at the low-temperature region between 2 K and 50 K, the resistivity curve can be well fitted by a power law T^{α} with $\alpha = 1.98$, close to the value 2, which is commonly observed in ferromagnetic metals.

Magnetoresistance (MR) measurements were carried out in conduction in-plane (CIP) geometry and with the external

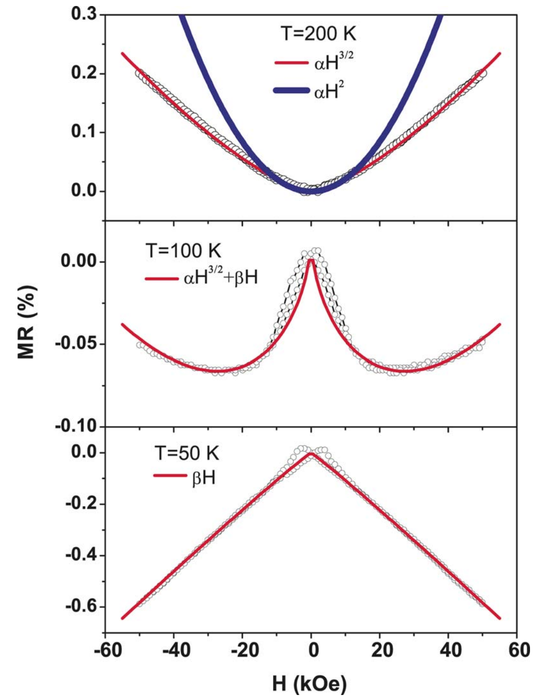

FIG. 10. (Color online) The magnetoresistance $\text{MR} = [\rho(H) - \rho(0)] / \rho(0)$ as a function of magnetic field measured at 200, 100, and 50 K, respectively. All data were taken in the magnetic field perpendicular to the film plane. The positive MR at 200 K and the negative MR at 50 K can be fitted qualitatively by $\alpha(T)H^{3/2}$ and $\beta(T)H$, respectively. The coefficients $\alpha(T)$ and $\beta(T)$ can be temperature dependent. Interestingly, at an intermediate temperature of 100 K, the MR response can be reproduced by superimposing the positive and negative MR responses—i.e., $\text{MR} \propto \alpha(T)H^{3/2} + \beta(T)H$.

magnetic field applied perpendicular to the film plane. Significant MR is observed, and three typical MR curves at temperatures of 200, 100, and 50 K are plotted in Fig. 10. The MR was calculated from the resistivity (ρ_{xx}) with and without a magnetic field and defined as $\text{MR} = [\rho_{xx}(0) - \rho_{xx}(H)] / \rho_{xx}(0)$. The value of MR at a temperature of 200 K, though small, is positive. It shows that the MR response has a simple relation with external magnetic fields (H) and can be described by $\text{MR} \propto \alpha(T)H^{3/2}$, where $\alpha(T)$ is a coefficient, which could be temperature dependent. However, at a temperature of 50 K, the signal of the MR is negative and follows a linear dependence on magnetic field with no evidence of saturation. That is, the relation between MR and magnetic field can be described by $\text{MR} \propto \beta(T)H$, where $\beta(T)$ is a coefficient, which could be temperature dependent. On the other hand, the structure of the MR at an intermediate temperature of 100 K appears to be composed of a sharp center negative MR feature (at low field) and out wings (at higher fields) reflecting a positive MR contribution to the total MR. Interestingly, we found that the relation between MR and magnetic field can be qualitatively described by $\text{MR} \propto \alpha(T)H^{3/2} + \beta(T)H$. This means that the MR response at 100 K can be reproduced as a sum of two components—i.e., positive MR at 200 K and negative MR at 50 K.

In Fig. 11, we display the temperature dependence of the MR under different magnetic fields. Despite the structure of

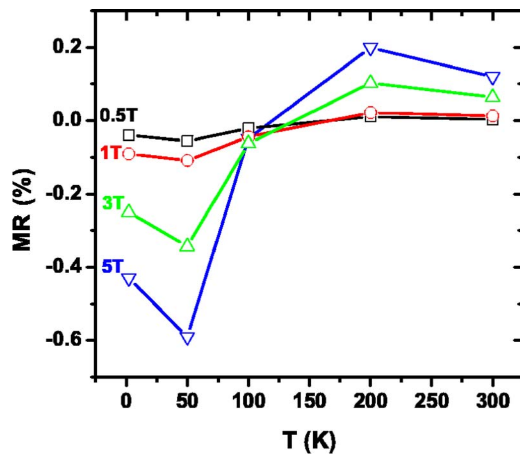

FIG. 11. (Color online) Temperature-dependent magnetoresistance at different applied magnetic fields.

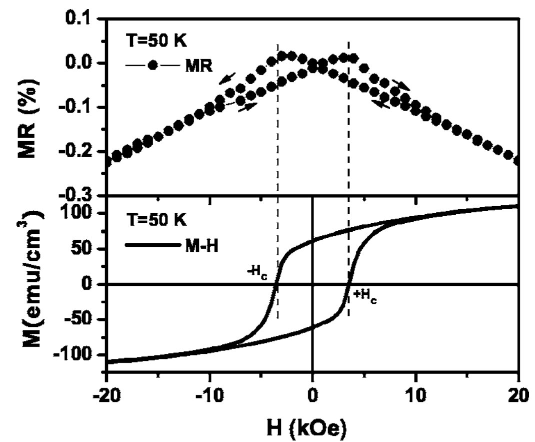

FIG. 12. Magnetoresistance (a) and magnetic hysteresis loop (b) measured at 50 K.

the MR, we found that at temperatures below 100 K, which is close to the local maximum in the resistivity curve shown in Fig. 9, the MR is negative. At temperatures higher than 100 K, a positive MR prevails. Phenomenologically, such kinds of temperature dependence, with a changed sign of the MR at a given temperature, could arise only from different temperature dependences of the positive and negative components to the total MR signal. Below the critical temperature of 100 K, the negative signal dominates over the positive signal, whereas above this temperature the positive signal dominates over the negative one.

The question arises as to the origin of the positive and negative components in our system. First we will discuss the possible origin of the positive MR. Usually, a positive MR is understood in terms of the Lorentz contribution to resistivity in the presence of magnetic field.[33] The magnitude of the positive MR induced by Lorentz force is proportional to the square of the magnetic field. However, as shown in Fig. 10(a), we found that the positive MR response is approximately proportional to $H^{3/2}$ rather than H^2. Furthermore, van Gorkom *et al.*[34] found that the positive MR induced by Lorentz force is strong at low temperatures and high magnetic fields, but it becomes smaller at higher temperatures. The positive MR ratio in Fig. 10(a) is much higher than that measured by van Gorkom *et al.*[34] We can therefore conclude that the positive MR induced by Lorentz force is too small to account for the MR variation in our sample. Another possible positive MR effect arises from quantum corrections (electron-electron interaction and weak localization effects) to the Boltzmann conductivity, as discussed by Sawicki *et al.*[35] in CdMnSe and Shapira *et al.*[36] for CdMnTe, or localization of holes on Mn impurities giving rise to an exponential dependence of the positive MR on the magnetic field. However, we can also rule out such a scenario because positive MR due to quantum corrections occurs more often at very low temperatures (usually below 5 K) and shows an exponential dependence versus H. (The positive MR in our sample is the $H^{3/2}$ dependence and occurs at temperatures higher than 100 K.) Finally, the possibility of spin-dependent scattering can be ruled out in the present case because the sign of the MR would be negative in the case of spin-dependent scattering. The observation of anomalous positive MR at high temperatures is, therefore, quite intriguing, and there is a need to explore other mechanisms to explain this finding.

Now we turn to explore the origin of the negative MR in our sample. In polaronic systems, one would expect the MR to be negative as the magnetic field aligns the polarons and thereby reduces the exchange barrier for activated hopping. Previously, negative MR results from spin-dependent scattering, which are typically observed in giant magnetoresistance materials, such as Fe/Cr multilayers.[37] Recently, Perkarek *et al.*[38] found that the iron-based nanoclusters in (In,Ga)As will show a negative MR contribution (3.2% at 5 K in 0.5 T) to a positive MR background. A small negative MR was also observed in granular MnAs:GaAs samples by Akinaga *et al.*[39] and attributed to spin-dependent scattering between MnAs clusters. In analogy with the above-mentioned magnetic metal/semiconductor multilayers and magnetic metal granular films, we expect that a spin-dependent scattering exists in our system. In Fig. 12, we show the MR curve measured at 50 K and corresponding hysteresis loop at the low-field region. A one-to-one correspondence can be clearly seen between these two curves, and this coincidence supports our assignment of the origin of the negative MR due to spin-dependent scattering. Furthermore, it is worth mentioning that, unlike the magnetization, the negative MR cannot be saturated and is nearly linear up to 5 T. A plausible explanation for the unsaturated negative MR is that the synthesized Mn-Si layer is a somewhat magnetically inhomogeneous medium containing nonaligned magnetic clusters on a microscopic scale. Upon increasing the magnetic field, these ultrafine magnetic clusters gradually align their magnetic moments with the external magnetic field, leading to a decrease in the spin-dependent resistance of the sample.

It is also noteworthy that a new MR mechanism for clustered inhomogeneities or embedded ferromagnetic nanoclusters in a nonmagnetic matrix has recently been proposed by Schmidt *et al.*[40] This mechanism emphasizes fluctuations in the magnitude and orientation of the magnetization of nanoclusters. A magnetic field suppresses these fluctuations and thereby reduces the probability that a trapped hole hops from

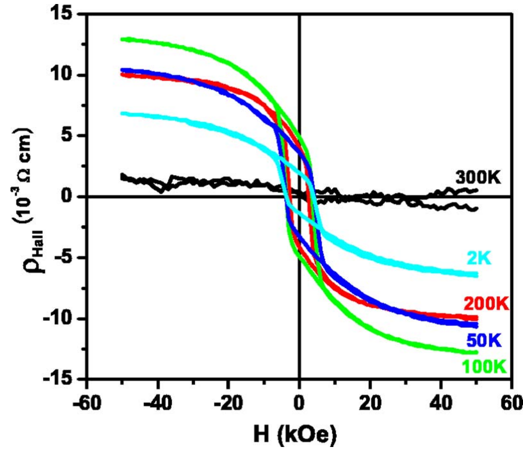

FIG. 13. (Color online) Field-dependent Hall resistivity ρ_{xy} as a function of magnetic field H ($H \perp$ thin film) at various temperatures.

one magnetic polaron site to another. Meanwhile, the magnetic field also reduces the polaron barrier; hence, both positive and negative MR effects could be observed by weighting disorder and occupation effects as a function of temperature and magnetic field. This interpretation is qualitatively consistent with the observed MR in this work, if the interstitial Mn atoms can be considered as highly conducting inclusions in a 4H-SiC semiconducting matrix in the interface. At this point, however, it is not clear why and how the ferromagnetic-superparamagnetic interface can influence the signal of total MR, since direct measurement of transport properties is impossible due to the very high resistivity in the etched sample. Nevertheless, a crossover of magnetoresistance from negative to positive has been recently observed in a heterojunction composed of (La,Ce)MnO_3/$SrTiO_3$ (Ref. 41) and also in (La,Ce)MnO_3/$SiTiO_3$/(La,Ca)MnO_3 tunneling junctions.[42] These results reveal that the ferromagnetic-nonmagnetic interface plays a key role in understanding the remarkable MR variations.

D. Anomalous Hall effect

The Hall resistivity (ρ_{xy}) in ferromagnetic metals can be commonly expressed as $\rho_{xy}=R_OB+R_S\mu_0M$,[43] where R_O and R_S are the ordinary and anomalous Hall coefficients, respectively, B is the magnetic field, and M is the magnetization. The first term (R_OB) denotes the ordinary Hall effect (OHE), and the second term ($R_S\mu_0M$) denotes the anomalous Hall effect (AHE). The AHE is proportional to M and conventionally originates from an asymmetric scattering process involving a spin-orbit interaction. The effect of the OHE usually appears in higher fields, while the measured Hall resisitivity is dominated by the AHE in lower fields. In Fig. 13, we show the results of the Hall resistivity ρ_{xy} as a function of magnetic field H ($H \perp$ thin film) at various temperatures. Unlike in nonmagnetic metals, the ρ_{xy} curves at low temperatures show a clearly nonlinear dependence on the magnetic filed, thus indicating that the measured Hall resistivity is dominated by the AHE in our sample. Furthermore, the ρ_{xy} curves in the high-magnetic-field region have a negative slope due to the OHE, which indicates n-type conduction.

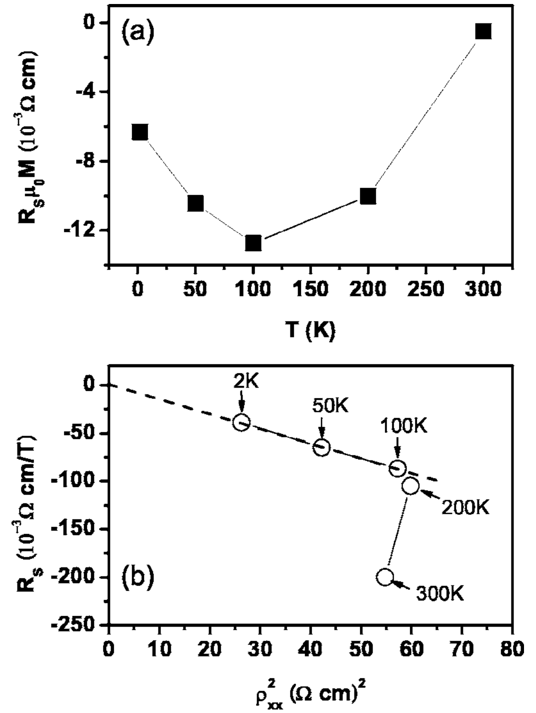

FIG. 14. (a) Temperature-dependent AHE part of the Hall resistivity and (b) the AHE coefficient R_S as a function of the longitudinal resistivity squared, ρ^2_{xx}.

Since ρ_{xy} is dominated by of the AHE in low fields, therefore the OHE contribution to the total Hall effect can be generally neglected. As a result we may reliably identify the AHE at each temperature from the intercept of the ρ_{xy} curve to zero field by assuming the OHE to be nearly temperature independent. Figure 14(a) shows the AHE resistivity ($R_S\mu_0M$) at $H=0$ as a function of temperature. We should point out that, as an example, we use a negative value of $R_S\mu_0M$, but the picture will be quantitatively the same for the positive one because only the signal is of concern here and ρ_{xy} curves are completely symmetric with respect to the magnetic fields (see Fig. 13). Very interestingly, $R_S\mu_0M$ has an unusual temperature-dependent behavior; that is, with increasing temperature, $R_S\mu_0M$ becomes more negative, reaching a minimum at about 100 K, after which it increases and eventually reaches zero at 300 K. Clearly, this temperature-dependent behavior cannot be understood using the traditional AHE theory,[43] which is predicted to be proportional to the magnetization and therefore should decrease monotonously with increasing temperature, reaching zero at T_c. Recently, Fang *et al.*[44] found that the AHE of metallic $SrRuO_3$ shows a nonmonotonous temperature dependence that even includes a sign change. We noted that a quite similar result is also observed in another sample synthesized by the carbonization technique, and a detailed comparison between experiments and theory will be given in a forthcoming paper. Moreover, the unusual temperature-dependent $R_S\mu_0M$ is reminiscent of a sign change observed in the temperature-dependent MR as shown in Fig. 11. Remarkably, the point where the AHE attains its minimum value is where MR $\rightarrow 0$: at the crossover from negative to positive character. Because of the strong correlation between AHE and MR, it

may be necessary in theory to treat both MR and AHE on an equal footing.

In the classical model of the AHE for ferromagnetic metals, R_S is given by $R_S = a\rho_{xx} + b\rho_{xx}^2$,[43] where ρ_{xx} is the longitudinal resistivity and a are b are constants. The linear term in ρ_{xx} is attributed to asymmetric skew scattering of charge carriers, a process which derives from the classical Boltzmann equation. On the other hand, the quadratic term in ρ_{xx} is attributed to asymmetric side jumps, which are a purely quantum scattering process. In Fig. 14(b) we plot R_S as a function of the resistivity square. We observe a discontinuity in R_S vs ρ_{xx}^2 at around 100 K. At low temperature (2–100 K), we can linear fit R_S by $R_S = b\rho_{xx}^2$. This means that the measured Hall effect is dominated by an AHE due to side jumps at temperatures between 2 K and 100 K. On the other hand, at temperatures higher than 100 K, the R_S cannot be fit with either a skew scattering or side jump mechanism. Recently, it was reported that the AHE of manganites,[45] which are strongly electron-correlated metals whose resistivity is dominated by magnetic disorder, cannot be fitted with either a skew scattering or side jump mechanism; however, the data were fitted quite well with new theoretical predictions that took into consideration the particular transport properties of these compounds.[46] Nevertheless, a quantitative analysis of AHE will be difficult because even the band structure of Mn_5Si_2 is still unclear at present. However, this experimentally identified temperature-dependent behavior would stimulate theoretical challenges to understand the band structure and AHE.

IV. CONCLUSION

We have studied the structural, magnetic, and magnetotransport properties of Mn-Si films synthesized on a 4*H*-SiC(0001) wafer, using fluorescence-extended x-ray-absorption fine-structure techniques and magnetization measurements. The observed room-temperature ferromagnetic behaviors are intrinsic properties of carbon-incorporated Mn_5Si_2, not coming from precipitates of other Mn-Si compounds. In the interlayer—i.e., between the top Mn_5Si_2 layer and SiC substrate—mostly Mn atoms are incorporated on the interstitial site in the SiC lattice and show a superparamagnetismlike behavior with a blocking temperature below 2 K. The magnetoresistance exhibits an interesting temperature- and magnetic-field-dependent behavior. At temperatures above 100 K, the sample only exhibits a positive MR. At temperatures below 100 K, a strong negative MR is observed. Since the positive MR induced by Lorentz force is too small to account for the MR variation in our sample, at this stage, we cannot explain the origin of the positive MR. On the other hand, the negative MR is mainly attributed to local magnetic disorder, undetectable magnetic clusters, and heterogeneity. Therefore, the origin of the negative MR is attributed to the spin-dependent scattering. We have also measured the Hall effect as a function of temperature and magnetic field. We found that the anomalous Hall effect can be described by a side jump mechanism at temperatures between 2 K and 100 K. Detailed theoretical studies are called for to explain the interface superparamagnetismlike properties and the intertwined relationship of the AHE and MR.

ACKNOWLEDGMENTS

The authors would like to thank K. Kojima (Power Electronics Research Center, AIST) for providing the 4*H*-SiC(0001) homoepitaxial wafers used in this study. W.H.W is grateful for financial support from the Japan Society for the Promotion of Science (JSPS). This work was partially supported by the Photon Factory Program Advisory Committee (Project No. 2006G069).

*Electronic address: wang.wenhong@aist.go.jp

[1] H. Ohno, Science **281**, 951 (1998).

[2] T. Dietl, Semicond. Sci. Technol. **17**, 377 (2002).

[3] H. Ohno, H. Munekata, T. Penney, S. von Molnar, and L. L. Chang, Phys. Rev. Lett. **68**, 2664 (1992).

[4] D. Ferrand, J. Cibert, A. Wasiela, C. Bourgognon, S. Tatarenko, G. Fishman, T. Andrearczyk, J. Jaroszynski, S. Kolesnik, T. Dietl, B. Barbara, and D. Dufeu, Phys. Rev. B **63**, 085201 (2001).

[5] T. Jungwirth, K. Y. Wang, J. Masek, K. W. Edmonds, J. Konig, J. Sinova, M. Polini, N. A. Goncharuk, A. H. MacDonald, M. Sawicki, R. P. Campion, L. X. Zhao, C. T. Foxon, and B. L. Gallagher, Phys. Rev. B **72**, 165204 (2005).

[6] H. Shimizu, T. Hayashi, T. Nishinaga, and M. Tanaka, Appl. Phys. Lett. **74**, 398 (1999).

[7] T. Hayashi, Y. Hashimoto, S. Katsumoto, and Y. Iye, Appl. Phys. Lett. **78**, 1691 (2001).

[8] Y. Ishiwata, M. Watanabe, R. Eguchi, T. Takeuchi, Y. Harada, A. Chainani, S. Shin, T. Hayashi, Y. Hashimoto, S. Katsumoto, and Y. Iye, Phys. Rev. B **65**, 233201 (2002).

[9] H.-M. Kim, N. M. Kim, C. S. Park, S. U. Yuldashev, T. W. Kang, and K. S. Chung, Chem. Mater. **15**, 3964 (2003).

[10] S. Cho, S. Choi, S. C. Hong, Y. Kim, J. B. Ketterson, B. J. Kim, Y. C. Kim, and J. H. Jung, Phys. Rev. B **66**, 033303 (2002).

[11] H. K. Kim, D. Kwon, J. H. Kim, Y. E. Ihm, D. Kim, H. Kim, J. S. Baek, C. S. Kim, and W. K. Choo, J. Magn. Magn. Mater. **282**, 244 (2004).

[12] F. M. Zhang, X. C. Liu, J. Gao, X. S. Wu, Y. W. Du, H. Zhu, J. Q. Xiao, and P. Chen, Appl. Phys. Lett. **85**, 786 (2004).

[13] Y. T. Zhang, Q. Jiang, D. J. Smith, and J. Drucker, J. Appl. Phys. **98**, 033512 (2005).

[14] Y. D. Park, A. T. Hanbicki, S. C. Erwin, C. S. Hellberg, J. M. Sullivan, J. E. Matson, T. F. Ambrose, A. Wilson, G. Spanos, and B. T. Jonker, Science **295**, 651 (2002).

[15] A. P. Li, J. Shen, J. R. Thompson, and H. H. Weitering, Appl. Phys. Lett. **86**, 152507 (2005); A. P. Li, J. F. Wendelken, J. Shen, L. C. Feldman, J. R. Thompson, and H. H. Weitering, Phys. Rev. B **72**, 195205 (2005).

[16] A. Ayvajarvi, L. Nasi, G. R. Yazdi, G. Salviati, M. Izadifard, I. A. Buyanova, W. M. Chen, and R. Yakimova, Mater. Sci. Forum **483**, 241 (2005).

[17] S. Dhar, O. Brandt, and K. H. Ploog, Appl. Phys. Lett. **86**, 112504 (2005).
[18] See, e. g., N. Theodoropoulou, A. F. Hebard, S. N. G. Chu, M. E. Overberg, C. R. Abernathy, S. J. Pearton, R. G. Wilson, J. M. Zavada, and Y. D. Park, J. Vac. Sci. Technol. A **20**, 578 (2002).
[19] See, e. g., V. A. Gubanow, C. Boekema, and C. Y. Fong, Appl. Phys. Lett. **78**, 216 (2001); M. S. Miao and W. R. L. Lambrecht, Phys. Rev. B **68**, 125204 (2003); Y. S. Kim, Y.-C. Chung, and S.-C. Yi, Mater. Sci. Eng., B **194–196**, 194 (2006).
[20] F. Takano, H. Akinaga, H. Ofuchi, S. Kuroda, and K. Takita, J. Appl. Phys. **99**, 08J506 (2006).
[21] D. Kwon, H. K. Kim, J. H. Kim, Y. E. Ihm, D. Kim, H. Kim, J. S. Baek, C. S. Kim, and W. Ki. Choo, J. Magn. Magn. Mater. **282**, 240 (2004).
[22] T. Takeuchi, M. Igarashi, Y. Hirayama, and M. Futamoto, J. Appl. Phys. **78**, 2132 (1995).
[23] R. Nakatani, T. Kusano, H. Yakame, and M. Yamamoto, Jpn. J. Appl. Phys., Part 1 **41**, 5978 (2002).
[24] C. Sürgers, H. v. Löhneysen, M. T. Kelemen, E. Dormann, and M. S. S. Brooks, J. Magn. Magn. Mater. **240**, 383 (2002).
[25] C. Sürgers, M. Gajdzik, G. Fischer, H. v. Löhneysen, E. Welter, and K. Attenkofer, Phys. Rev. B **68**, 174423 (2003).
[26] T. Ohno, H. Yamaguchi, S. Kuroda, K. Kojima, T. Suzuki, and K. Arai, J. Cryst. Growth **260**, 209 (2004).
[27] W. H. Wang, F. Takano, H. Ofuchi, and H. Akinaga, J. Cryst. Growth **301**, 607 (2007).
[28] L. Ritchie, G. Xiao, Y. Ji, T. Y. Chen, C. L. Chien, M. Zhang, J. L. Chen, Z. H. Liu, G. H. Wu, and X. X. Zhang, Phys. Rev. B **68**, 104430 (2003).
[29] Z. H. Liu, H. N. Hu, G. D. Liu, Y. T. Cui, M. Zhang, J. L. Chen, G. H. Wu, and G. Xiao, Phys. Rev. B **69**, 134415 (2004).
[30] W. H. Wang, M. Przybylski, W. Kuch, L. I. Chelaru, J. Wang, Y. F. Lu, J. Barthel, H. L. Meyerheim, and J. Kirschner, Phys. Rev. B **71**, 144416 (2005).
[31] B. Heinrich and J. F. Cochran, Adv. Phys. **42**, 523 (1993).
[32] H. Ofuchi, W. H. Wang, F. Takano, and H. Akinaga (unpublished).
[33] J. P. Jan, Solid State Phys. **5**, 1 (1957).
[34] R. P. van Gorkom, J. Caro, T. M. Klapwijk, and S. Radelaar, Phys. Rev. B **63**, 134432 (2001).
[35] M. Sawicki, T. Dietl, J. Kossut, J. Igalson, T. Wojtowicz, and W. Plesiewicz, Phys. Rev. Lett. **56**, 508 (1986).
[36] Y. Shapira, N. F. Oliveira, P. Becla, and T. Q. Vu, Phys. Rev. B **41**, 5931 (1990).
[37] M. N. Baibich, J. M. Broto, A. Fert, F. Nguyen Van Dau, F. Petroff, P. Etienne, G. Creuzet, A. Friederich, and J. Chazelas, Phys. Rev. Lett. **61**, 2472 (1988).
[38] A. T. M. Pekarek, B. V. Crooker, S. Li, M. McElifresh, J. C. P. Chang, D. McInturff, E. S. Harmon, M. R. Melloch, and J. M. Woodall, J. Appl. Phys. **81**, 4869 (1997).
[39] H. Akinaga, J. De Boeck, G. Borghs, S. Miyanishi, A. Asamitsu, W. Van Roy, Y. Tomioka, and L. H. Kuo, Appl. Phys. Lett. **72**, 3368 (1998).
[40] D. R. Schmidt, A. G. Petukhov, M. Foygel, J. P. Ibbetson, and S. J. Allen, Phys. Rev. Lett. **82**, 823 (1999).
[41] Z. G. Sheng, W. H. Song, Y. P. Sun, J. R. Sun, and B. G. Shen, Appl. Phys. Lett. **87**, 032501 (2005).
[42] C. Mitra, P. Raychaudhuri, K. Dorr, K.-H. Muller, L. Schultz, P. M. Oppeneer, and S. Wirth, Phys. Rev. Lett. **90**, 017202 (2003).
[43] For a review see, e. g., C. M. Hurd, *The Hall Effect in Metals and Alloys* (Plenum, New York, 1972); *The Hall Effect and its Applications*, edited by C. L. Chien and C. R. Westgate (Plenum, New York, 1980), and references therein.
[44] Z. Fang, N. Nagaosa, K. S. Takahashi, A. Asamitsu, R. Mathieu, T. Ogasawara, H. Yamada, M. Kawasakik, Y. Tokura, and K. Terakura, Science **302**, 92 (2003).
[45] Y. Lyanda-Geller, S. H. Chun, M. B. Salamon, P. M. Goldbart, P. D. Han, Y. Tomioka, A. Asamitsu, and Y. Tokura, Phys. Rev. B **63**, 184426 (2001).
[46] S. H. Chun, M. B. Salamon, Y. Lyanda-Geller, P. M. Goldbart, and P. D. Han, Phys. Rev. Lett. **84**, 757 (2000).